

Speaker-wire vortices in stratified anabatic Prandtl slope flows and their secondary instabilities

Cheng-Nian Xiao¹ and Inanc Senocak^{1,†}

¹Department of Mechanical Engineering and Materials Science, University of Pittsburgh, 3700 O'Hara St, Pittsburgh, PA 15261, USA

(Received 20 January 2022; revised 31 May 2022; accepted 1 June 2022)

Stationary longitudinal vortical rolls emerge in katabatic and anabatic Prandtl slope flows at shallow slopes as a result of an instability when the imposed surface buoyancy flux relative to the background stratification is sufficiently large. Here, we identify the self-pairing of these longitudinal rolls as a unique flow structure. The topology of the counter-rotating vortex pair bears a striking resemblance to speaker-wires and their interaction with each other is a precursor to further destabilization and breakdown of the flow field into smaller structures. On its own, a speaker-wire vortex retains its unique topology without any vortex reconnection or breakup. For a fixed slope angle $\alpha = 3^\circ$ and at a constant Prandtl number, we analyse the saturated state of speaker-wire vortices and perform a bi-global linear stability analysis based on their stationary state. We establish the existence of both fundamental and subharmonic secondary instabilities depending on the circulation and transverse wavelength of the base state of speaker-wire vortices. The dominance of subharmonic modes relative to the fundamental mode helps to explain the relative stability of a single vortex pair compared to the vortex dynamics in the presence of two or an even number of pairs. These instability modes are essential for the bending and merging of multiple speaker-wire vortices, which break up and lead to more dynamically unstable states, eventually paving the way for transition towards turbulence. This process is demonstrated via three-dimensional flow simulations with which we are able to track the nonlinear temporal evolution of these instabilities.

Key words: buoyancy-driven instability, stratified flows, vortex instability

1. Introduction

The Prandtl model for katabatic and anabatic slope flows serves as a canonical model to comprehend the main dynamics of stably stratified flows around complex terrain, such

† Email address for correspondence: senocak@pitt.edu

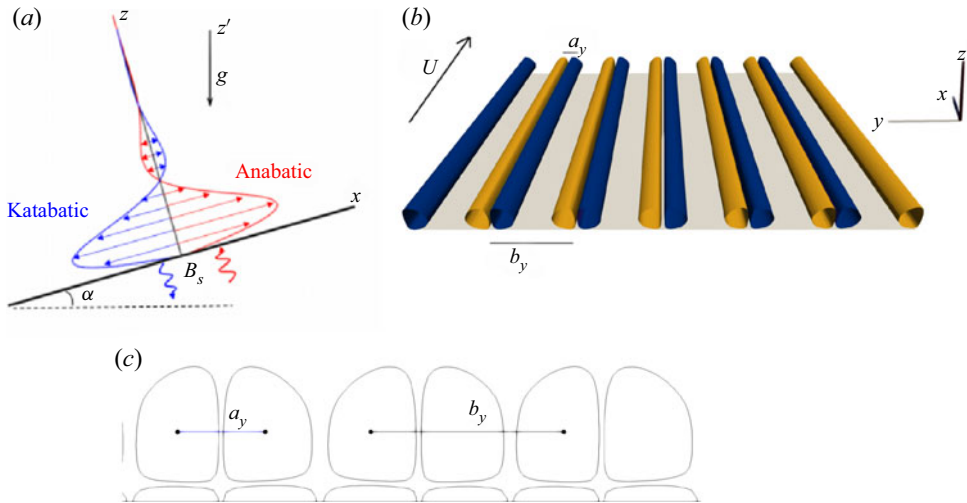


Figure 1. Base flow profiles for slope flows under Prandtl's model. (a) Sketch of slope flow geometry and the rotated coordinate system. (b) Longitudinal vortex pairs (speaker-wire vortices) arising as instability of the laminar anabatic (up-slope) Prandtl flow U , with definition of coordinate axes, roll separation a_y , and speaker-wire vortex separation b_y , which is equivalent to the transverse wavelength of the (primary) linear instability. (c) Two-dimensional view of three speaker-wire vortex pairs, with indications of the roll separation a_y and vortex (pair) separation b_y .

as mountains and valleys (Prandtl 1942, 1952). The Prandtl model possesses analytical one-dimensional (1-D) laminar flow solutions that are exponentially damped sinusoidal velocity and buoyancy profiles along the slope-normal direction (Shapiro & Fedorovich 2004; Fedorovich & Shapiro 2009). The solution gives rise to a strong near-surface jet along the slope direction capped by a weak reverse flow, as illustrated in figure 1.

In recent studies, we have investigated the linear stability of the Prandtl model for katabatic (Xiao & Senocak 2019) and anabatic (Xiao & Senocak 2020*b*) slope flows, as well as the extended version of the Prandtl model with ambient winds (Xiao & Senocak 2020*a*), and discovered the existence of a stationary roll instability at small slope angles, and a travelling wave instability at steeper slopes. These studies have also helped to establish the importance of the dimensionless stratification perturbation parameter in controlling the dynamics of stably stratified slope flows.

In the present investigation, we are interested in the progression of stationary roll instabilities in anabatic slope flows towards dynamically more unstable states. Despite accumulating experimental and numerical results in understanding turbulence structure in neutral and unstable flows, the transition to turbulence under stable conditions still leaves open many significant questions.

Vortex pairing, which in its simplest form is a purely two-dimensional (2-D) dynamics where neighbouring vortices merge with each other, has been studied experimentally while observing shear-layer growth (Winant & Browand 1974). In related experiments, Miksad (1972) demonstrated that 2-D vortex structures are susceptible to three-dimensional (3-D) instabilities. These 3-D vortex instabilities are responsible for the creation of irregular flow at smaller scales which, however, do not impact significantly the large-scale vortex structures (Browand & Weidman 1976). The vortex instabilities are thus crucial for the transition from 2-D to 3-D flows, and they continue to shape the features of the turbulent flow that develops further downstream. The simultaneous existence of stratification and

bounding surface(s) is expected to complicate the picture further, as outlined above. However, there have been few theoretical approaches to adequately model vortex dynamics under these additional flow conditions that are encountered frequently in real life.

For configurations without solid boundaries, Crow (1970) conducted a stability analysis for a pair of parallel counter-rotating vortices in neutrally stable as well as quiescent ambient air, and found sinusoidal symmetric bending of each vortex, which eventually led to the reconnection and vortex ring formation at locations where the distance between the neighbouring vortices became minimal. The linear stability of counter-rotating vortex arrays in homogeneous fluid as introduced by Mallier & Maslowe (1993) has been analysed in a numerical study limited to two spatial dimensions by Dauxois, Fauve & Tuckerman (1996), which has been later extended to three dimensions by Julien, Chomaz & Lasheras (2002). These works, however, only focused on fundamental instabilities with the same wavelength as the base vortex array. The 3-D long-wave instabilities of well-separated vortex arrays have been studied by Robinson & Saffman (1982), which utilized the same approach as Crow (1970) and focused on cooperative modes due to mutual induction only. This analysis has been extended to study vortex instability in rotating and stratified fluids by Deloncle, Billant & Chomaz (2011).

Elliptic instabilities, which lead to anti-symmetric deformation of vortex cores, were observed for vortices with non-circular streamlines (Pierrehumbert 1986; Schmid & Henningson 2001; Hattori *et al.* 2021) and are caused by resonance of inertial vortex waves with the local flow strain; however, they are suppressed by the presence of stable stratification, as shown by Miyazaki & Fukumoto (1992). On the other hand, Le Dizès & Billant (2009) have shown that a single vertical columnar vortex can be unstable at stably stratified conditions due to the propagation and resonance of internal gravity waves, which is termed a radiative instability. The dynamics of short-wavelength elliptic instability of co-rotating and counter-rotating vortex pairs in the presence of axial flows has been studied with direct numerical simulations by Roy *et al.* (2008), who found that axial flows tend to weaken the nonlinear dynamics of the elliptic instability.

Another type of vortex instability that exists in rotating flows under stably stratified conditions is the so-called zig-zag instability, which was first discovered and analysed by Billant & Chomaz (2000) and Billant (2010), and should not be confused with the zig-zag instabilities coined in Clever & Busse (1974) to describe 3-D instabilities of steady convection rolls. The former type of zig-zag instabilities are caused by additional self-induction as well as mutual induction among well-separated vortices due to a background density gradient that is aligned with the main columnar vortex, and they lead to symmetric vortex bending in well-separated co-rotating vortex pairs and anti-symmetric bending in counter-rotating pairs.

Besides studying the dynamics of the above-mentioned model vortices that arise as approximate or exact solutions of the Navier–Stokes equations, a second line of investigation has focused on stability analysis for roll structures that emerge as primary instability due to thermal convection or shear. Corcos & Sherman (1984) have identified that instabilities of vortices, which themselves arise as a primary instability in a 1-D shear layer, are responsible for vortex mergers and turbulence transition. The stability of convection rolls that form on flat as well as inclined heated surfaces in the absence of any stratification effects has been studied by Clever & Busse (1974, 1977) and Busse & Clever (1979), which led to the discovery of the famous ‘Busse balloon’ within the parameter space spanned by the horizontal wavenumber and Rayleigh number where these convection rolls are dynamically stable. Similar stability analysis has been carried out for Görtler vortices under neutrally stratified conditions, and fundamental as well as

subharmonic instability modes have been discovered by Hall & Horseman (1991) and Li & Malik (1995). Like the results by Pierrehumbert & Widnall (1982) for co-rotating Stuart vortices, Li & Malik (1995) found that the fundamental modes cause a synchronous displacement of adjacent Görtler vortices, whereas the subharmonic modes lead to either merging or separation of two neighbouring vortices. All the research listed above has focused on the dynamics of elementary configurations with no more than two vortices, which are either counter-rotating (single vortex pair) or co-rotating (subharmonic mode of vortex array). However, the stability of stratified vortex configurations in the presence of a solid boundary involving more than two vortices, whether of the same sense of rotation or not, has found little attention so far.

In the present work, we expand our investigation of Prandtl's stratified slope flows with stability analysis of the steady vortex pair arrays that arise as the saturated steady state of the primary instability under an anabatic heating condition at shallow slopes. From now on, each counter-rotating vortex pair will be designated as a speaker-wire vortex, and the motivation behind this terminology will be explained in more detail later. There are several major differences between the instabilities of these speaker-wire vortices under Prandtl's model and the other well-known vortex instabilities that we have mentioned above, such as Crow's instability, elliptic instability, zig-zag instability, secondary convection rolls and Görtler instabilities. Most importantly, the flow configuration described by Prandtl's model includes the following key components: first, a constant vertical stable stratification that is at an oblique angle to the longitudinal rolls aligned with the streamwise direction, and second, a solid wall boundary with its associated boundary layer of the Prandtl base flow. The simultaneous presence of both features makes an analytical treatment very challenging and, to the best of our knowledge, is absent in the published literature. As discovered in our earlier works (Xiao & Senocak 2019, 2020b), the primary roll instability of Prandtl's base flow consists of a pair of two counter-rotating vortices, hence any subharmonic secondary instability must involve at least two such pairs and four vortices in total, which is larger than the typical number of vortices (1 or 2) in base flow configurations that have been investigated in the current literature on stability analysis. Similar to the approach that we have pursued in Xiao & Senocak (2019), we apply linear bi-global stability analysis to identify the different modes that can destabilize the base flow vortices. Further, we conduct analyses to determine how these modes may depend on external flow conditions and their role in the turbulence transition of slope flows.

2. Properties of speaker-wire vortices

2.1. Governing equations

Let us consider the idealized Prandtl slope flow configuration as shown in figure 1(a), where α is the slope angle, and gravity \mathbf{g} acts downwards in the vertical direction. A constant positive buoyancy flux B_S is imposed at the surface. We consider a rotated Cartesian coordinate system whose x axis is aligned with the planar inclined surface. The direction normal to the slope surface is represented by the z component of the position vector, whereas the cross-flow transverse direction is aligned with the y coordinate. Let u be the along-slope (longitudinal), v the cross-slope (transverse), and w the slope-normal velocity components, such that $\mathbf{u} = u_i = [u, v, w]$ is the velocity vector. The normalized gravity vector in the rotated coordinate system is then given by $g_i = (g_1, g_2, g_3) = [\sin \alpha, 0, \cos \alpha]$.

The potential temperature, buoyancy and Brunt–Väisälä frequency are denoted by Θ , b and N , respectively, where N , which is assumed to be constant under Prandtl’s model, is related to the potential temperature as $N = \sqrt{(g/\Theta_r)(\partial\Theta_e/\partial z')}$ and quantifies the background stratification, with z' denoting the vertical height with respect to the horizontal. The buoyancy is defined as a perturbation potential temperature as $b = g(\Theta - \Theta_e)/\Theta_r$, where Θ_r is a reference potential temperature, and Θ_e is the environmental (ambient) potential temperature. The kinematic viscosity and thermal diffusivity of the fluid are denoted by ν and β , respectively, and they are assumed to be constant. The transport equations for momentum with a Boussinesq approximation and buoyancy fields are written as

$$\frac{\partial \mathbf{u}}{\partial t} + \nabla \cdot (\mathbf{u} \otimes \mathbf{u}) = -\frac{1}{\rho} \nabla p + b \mathbf{n}_\alpha + \nu \Delta \mathbf{u}, \tag{2.1}$$

$$\frac{\partial b}{\partial t} + \nabla \cdot (b\mathbf{u}) = \beta \Delta b - N^2(\mathbf{n}_\alpha \cdot \mathbf{u}), \tag{2.2}$$

where $\mathbf{n}_\alpha = (\sin \alpha, 0, \cos \alpha)$ is the slope-normal unit vector. The conservation of mass principle is imposed by a divergence-free velocity field:

$$\nabla \cdot \mathbf{u} = 0. \tag{2.3}$$

We impose a positive buoyancy flux B_s at the no-slip bottom surface, and impose periodic boundary conditions on the lateral boundaries. The top boundary satisfies the free-slip condition, which means that the normal gradients of buoyancy and slope-normal as well as the transverse velocity components are zero, whereas the vertical velocity component is set to zero.

For the 1-D laminar flow problem, Shapiro & Fedorovich (2004) extended the exact solution of Prandtl (1942) to include a constant surface flux instead of a constant buoyancy, and the following characteristic flow scales have been introduced in Fedorovich & Shapiro (2009):

$$l_0 = Pr^{-1/4} \nu^{1/2} N^{-1/2} \sin^{-1/2} \alpha, \tag{2.4}$$

$$u_0 = Pr^{1/4} \nu^{-1/2} N^{-3/2} B_s \sin^{-1/2} \alpha, \tag{2.5}$$

$$b_0 = Pr^{3/4} \nu^{-1/2} N^{-1/2} B_s \sin^{-1/2} \alpha, \tag{2.6}$$

where $Pr = \nu/\beta$ is the Prandtl number. A time scale $t_0 := l_0/|u_0| = \sqrt{\nu\beta} NB_s^{-1}$ and shear scale $S_0 := |u_0|/l_0 = \sqrt{Pr/\nu} N^{-1} B_s$ can also be defined from the above scales. We observe from (2.4)–(2.6) that the length scale characterizing the laminar boundary layer thickness is independent of the surface flux B_s , whereas the magnitude of both the reference velocity and buoyancy scale varies linearly with B_s . For all 3-D Navier–Stokes simulations, we use rectangular mesh elements and ensure in the discretization at least two points to resolve the length scale l_0 along both vertical and lateral directions. Subsequently, these characteristic scales will be applied to normalize all flow equations and quantities presented herein. Specifically, the stratification perturbation number Π_s as introduced in Xiao & Senocak (2019) can be regarded as the imposed surface buoyancy flux B_s normalized by the background stratification scale βN^2 . This unique parameter is

determined from the given external flow parameters as

$$\Pi_s \equiv \frac{B_s}{\beta N^2}. \quad (2.7)$$

As can be seen from the previous work on slope flows by Fedorovich & Shapiro (2009), there exists a simple relation between the Reynolds number Re based on the flow scales defined above and the parameter Π_s , which is given by $Re = \Pi_s \sin(\alpha)/Pr$. We should note that a Reynolds number does not arise naturally in Prandtl slope flows because there is no external length or velocity scale imposed on the flow, whereas Π_s arises naturally from an application of the Buckingham- π theorem. Furthermore, the significance of Π_s is not confined to stratified slope flows only. In Xiao & Senocak (2022), we have shown that Π_s emerges as an independent dimensionless parameter in open channel flows stratified simultaneously by a surface cooling flux and an independent ambient stratification.

2.2. Longitudinal rolls and mode selection for the transverse wavelength

The 1-D laminar Prandtl flow profile is susceptible to multiple types of linear instabilities when the surface buoyancy flux magnitude relative to the ambient stratification is sufficiently large, as characterized by the dimensionless number $\Pi_s = B_s/(\beta N^2)$ (cf. Xiao & Senocak 2020b). As shown in Xiao & Senocak (2020b), at shallow slopes such as $\alpha = 3^\circ$, the most dominant linear instability is a stationary mode leading to longitudinal vortices aligned along the streamwise direction within the main up-slope flow. For each Π_s , there exists an optimal wavelength $\lambda_{max}(\Pi_s)$ that decreases with increasing Π_s where the instability attains its maximal growth rate. Thus at a specified Π_s and for a given simulation domain with transverse length Y that is an integer multiple of this optimal wavelength, i.e. $Y = n\lambda_{max}(\Pi_s)$, $n \in \mathbb{N}$, the longitudinal rolls that arise as a result of linear instability have exactly this optimal transverse wavelength because modes of different wavelengths are out-competed due to their lower growth rates. Similarly, for any other arbitrary transverse domain length Y , the emerging longitudinal roll instability has wavelength $\lambda_y = (1/N)Y$, i.e. an integer fraction of the transverse length Y , and also possesses the maximal growth rate among all modes that fits an integer number of times into Y . Hence, by specifying the stratification perturbation Π_s and the transverse domain size Y in a simulation, we have predetermined both the wavelength λ_y of the emerging longitudinal rolls and the number N of full rolls that are contained along the transverse extent. We will make use of this technique throughout this study to generate vortex pairs with a desired wavelength λ_y , which also equals the distance between adjacent vortex pairs (see figures 1b and 1c).

2.3. Speaker-wire vortex structure at the saturated state

The 2-D version of the slope flow equations (2.1)–(2.3) where the along-slope direction is ignored, with imposed buoyancy flux B_s at the no-slip bottom surface, can be solved via any time-stepping method to arrive at the steady vortices that arise as a saturated linear instability for slope angles less than 9° when Π_s is sufficiently large (Xiao & Senocak 2020b). To reproduce conditions of the local linear stability analysis presented in Xiao & Senocak (2020b), the initial flow field is set to be the laminar Prandtl flow profile superposed with a weak sinusoidal disturbance varying along the transverse y direction. The evolution of the flow field is tracked until a quasi-steady state is reached, which produces stationary vortex structures as a result of nonlinear saturation of the growing

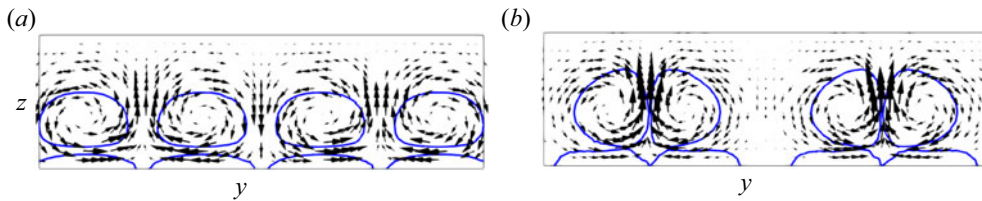


Figure 2. Speaker-wire vortices as a result of linear instability of the laminar anabatic Prandtl slope flow at $\alpha = 3^\circ$, with $\Pi_s = 2.0$ and initial transverse wavenumber $k_y = 1.22$: (a) during the linear growth phase of initial harmonic disturbances; and (b) in steady state after nonlinear saturation. The blue lines are streamwise vorticity magnitude contours, whereas the black arrows represent the velocity field projected onto the transverse yz plane.

initial disturbance at sufficiently large Π_s value. We would like to point out that despite the existence of vortex instabilities of the saturated speaker-wire vortices as described below, these will be triggered only when very specific types of initial disturbances with the proper wavelengths, such as those close to the strongest eigenmodes, are already present within the flow field. In our simulations, we used regular rectangular mesh elements that mostly suppress noisy numerical errors, thus allowing for the base vortices to develop and saturate without being subject to vortex instabilities as described below.

A comparison between the vortex structure during the linear growth phase and the final steady state is shown in figures 2(a) and 2(b). It is evident that even though the total number of vortex pairs (i.e. two) along the transverse direction has remained the same throughout, the originally uniformly distributed vortices have coalesced into one of their neighbours that has an opposite sense of rotation while moving away from their other neighbour, thus creating two counter-rotating pairs that are clearly separated from each other. We will refer to these vortex pairs as a speaker-wire vortex system, or more simply a speaker-wire vortex, due to their striking resemblance to actual speaker-wires. The anti-parallel neighbour of a given vortex (longitudinal roll) within the same speaker-wire vortex (pair) will be called its sister roll.

A measure of the nonlinear modification of the original uniform vortex structure is the width-to-spacing ratio $r = a_y/b_y$ between sister roll separation a_y and speaker-wire vortex (pair) separation b_y , as shown earlier in figure 1(b). For the initial disturbance varying harmonically along the y direction, $r = r_0 = 1/2$, and for the increased vortex separation as shown in figure 2(b), the value of r has decreased below r_0 . Clearly, the smaller the value of r , the more inhomogeneous the nonlinearly saturated vortices have become. This observation motivates the introduction of the vortex packing ratio (VPR) defined as $VPR = 2r = 2a_y/b_y \times 100\%$, which measures how close two adjacent speaker-wire vortices are from each other. During the linear growth phase, the rolls are distributed uniformly along the transverse direction with $r = 1/2$, thus $VPR = 100\%$ is maximal. When the rolls start to coalesce into pairs to form speaker-wire vortices, the VPR decreases due to clustering of two rolls within a pair. In the following, base speaker-wire vortices with VPR 70% or above will be regarded as tightly packed, those with VPR between 50% and 60% are called intermediately packed, and configurations whose VPR is less than 50% are classified as loosely packed.

Figure 3(a) shows the width-to-spacing ratio r as a function of the transverse wavelength λ_y of the primary roll instability, which equals the vortex separation b_y , at constant Π_s . The main vorticity magnitude at the vortex centre of the steady state longitudinal rolls as a function of λ_y is shown in figure 3(b) for different values of Π_s . It should be pointed

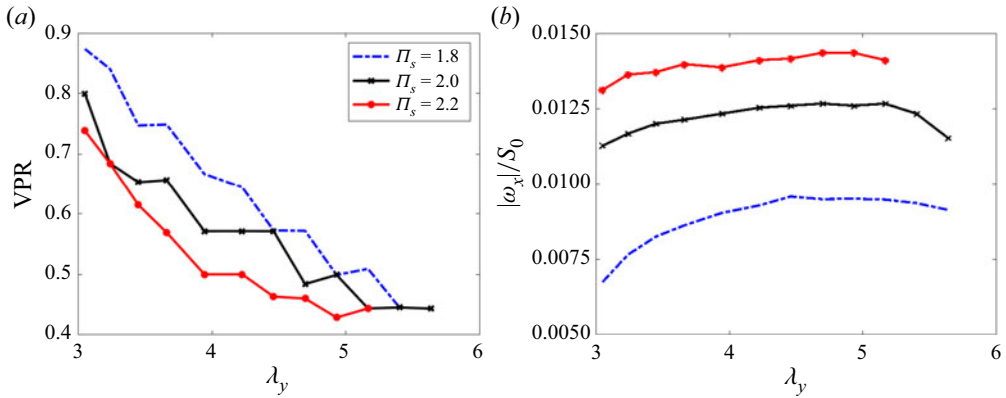


Figure 3. Characteristics of longitudinal vortex rolls for different values of Π_s after saturation from linear instability growth as a function of the transverse wavelength λ_y of the primary roll instability. (a) Vortex packing ratio (VPR), which is related to the width-to-spacing ratio r via $r = a_y/b_y = \frac{1}{2}VPR$, and $b_y = \lambda_y$ is the vortex separation. (b) Maximal streamwise vorticity magnitude $|\omega_x|$ normalized by characteristic shear S_0 .

out that since the longitudinal rolls are the manifestation of a primary instability, the roll separation a_y and vortex (pair) separation b_y are functions of the transverse domain size, which specifies the wavelength λ_y of the emerging primary instability via the mode selection mechanism that we describe in § 2.2. Thus at a fixed Π_s , the roll separation a_y and vortex (pair) separation b_y , as well as the centre vorticity, are not independent from each other; one can specify the value for only one of them by choosing the primary roll instability mode with the appropriate transverse wavelength λ_y , which then automatically fixes the other quantities of the emerging speaker-wire vortex structure. The dynamics of these speaker-wire vortices is unlike the vortex instabilities presented in the works of Pierrehumbert & Widnall (1982) and Crow (1970) in which the characteristics of the base flow vortices such as width and circulation can be specified freely, and these vortices are not a product of a prior instability. For significantly larger transverse domain sizes as shown here, the creation of an additional speaker-wire vortex will be favoured, whereas for smaller transverse domain sizes, there is favourable pressure for two existing speaker-wire vortices to merge into one. Thus the mode selection mechanism described earlier, in § 2.2, aims to modify the number of flow vortices that fit within the specified transverse domain size to arrive at a mode with larger growth rate at a different wavelength λ_y , which is an integer fraction of the transverse domain extent. This can also be regarded as a 2-D instability of the speaker-wire vortices, which will be explained in more detail in the following sections.

3. Linear secondary instability analysis of speaker-wire vortices

Let (U, V, W, B) be the flow field in 2-D space of the steady longitudinal rolls, and assuming that disturbances to this base flow are waves of the form

$$\mathbf{q}(x, y, z, t) = [\hat{u}(y, z), \hat{v}(y, z), \hat{w}(y, z), \hat{p}(y, z), \hat{b}(y, z)] \exp(ik_x x + \omega t), \quad (3.1)$$

then the resulting linearized equations have the following form:

$$ik_x \hat{u} + \frac{\partial \hat{v}}{\partial y} + \frac{\partial \hat{w}}{\partial z} = 0, \quad (3.2)$$

Speaker-wire vortices in stratified anabatic slope flows

$$\begin{aligned} \omega \hat{u} + iUk_x \hat{u} + \frac{\partial U}{\partial y} \hat{v} + \frac{\partial U}{\partial z} \hat{w} + \frac{\partial \hat{u}}{\partial y} V + \frac{\partial \hat{u}}{\partial z} W \\ = -ik_x \hat{p} - \frac{Pr}{\Pi_s} \sin \alpha \left(-k_x^2 \hat{u} + \frac{\partial^2 \hat{u}}{\partial y^2} + \frac{\partial^2 \hat{u}}{\partial z^2} + \hat{b} \right), \end{aligned} \quad (3.3)$$

$$\begin{aligned} \omega \hat{v} + iUk_x \hat{v} + \frac{\partial V}{\partial y} \hat{v} + \frac{\partial V}{\partial z} \hat{w} + \frac{\partial \hat{v}}{\partial y} V + \frac{\partial \hat{v}}{\partial z} W \\ = -\frac{\hat{p}}{\partial y} - \frac{Pr}{\Pi_s} \sin \alpha \left(-k_x^2 \hat{v} + \frac{\partial^2 \hat{v}}{\partial y^2} + \frac{\partial^2 \hat{v}}{\partial z^2} \right), \end{aligned} \quad (3.4)$$

$$\begin{aligned} \omega \hat{w} + iUk_x \hat{w} + \frac{\partial W}{\partial y} \hat{v} + \frac{\partial W}{\partial z} \hat{w} + \frac{\partial \hat{w}}{\partial y} V + \frac{\partial \hat{w}}{\partial z} W \\ = -\frac{\partial \hat{p}}{\partial z} - \frac{Pr}{\Pi_s} \sin \alpha \left(-k_x^2 \hat{w} + \frac{\partial^2 \hat{w}}{\partial y^2} + \frac{\partial^2 \hat{w}}{\partial z^2} + \hat{b} \cot \alpha \right), \end{aligned} \quad (3.5)$$

$$\begin{aligned} \omega \hat{b} + iUk_x \hat{b} + \frac{\partial B}{\partial y} \hat{v} + \frac{\partial B}{\partial z} \hat{w} + \frac{\partial \hat{b}}{\partial y} V + \frac{\partial \hat{b}}{\partial z} W \\ = -\frac{\sin \alpha}{\Pi_s} \left(-k_x^2 \hat{b} + \frac{\partial^2 \hat{b}}{\partial y^2} + \frac{\partial^2 \hat{b}}{\partial z^2} - (\hat{u} + \hat{w} \cot \alpha) \right), \end{aligned} \quad (3.6)$$

where \hat{u} , \hat{v} , \hat{w} , \hat{p} , \hat{b} are flow disturbances varying along the slope-normal and transverse directions normalized by the flow scales given in (2.4)–(2.6). The slope angle is fixed at $\alpha = 3^\circ$, whereas the normalized base flow field describing the steady vortices is denoted by (U, V, W, B) and is obtained via the simulation procedure described above.

The linearized equations for bi-global stability analysis can be written as a generalized eigenvalue problem as

$$\mathbf{A}(k_x) \hat{\mathbf{q}}(y, z) = \omega \mathbf{B}(k_x) \hat{\mathbf{q}}(y, z). \quad (3.7)$$

The 2-D complex disturbance vector

$$\hat{\mathbf{q}}(y, z) = [\hat{u}(y, z), \hat{v}(y, z), \hat{w}(y, z), \hat{p}(y, z), \hat{b}(y, z)]^T \quad (3.8)$$

varies in the slope-normal (z) and transverse (y) directions, where $(\hat{u}, \hat{v}, \hat{w})$ are the along-slope, cross-slope (transverse) and slope-normal disturbance velocity components. As a bi-global stability analysis, the slope-normal and transverse dimensions are fully resolved, and the disturbance variation along the streamwise direction is approximated by only one single Fourier mode with wavenumber k_x . When k_x is zero, then the corresponding mode is 2-D without any streamwise variation, whereas a positive k_x implies a full 3-D disturbance. The appropriate boundary conditions for this problem are no-slip for disturbance velocities at $z = 0$ and $z \rightarrow \infty$, and for buoyancy disturbance, $\partial \hat{b} / \partial z|_0 = 0$ and $\hat{b}|_{z \rightarrow \infty} = 0$ are imposed. The slope-normal derivative of pressure disturbance \hat{p} is also set to zero at both $z = 0$ and $z \rightarrow \infty$. On both transverse boundaries $y = 0$ and $y = \lambda_y = b_y$, periodic conditions are imposed for all variables. The generalized eigenvalue problem (3.7) is discretized via spectral elements in the transverse plane, which is available in Nektar++ (Cantwell *et al.* 2015). For a base flow containing two full transverse spatial periods, i.e. two speaker-wire vortices, around 150 degrees of freedom

are used for discretization in each transverse direction, and the resulting generalized eigenvalue problem is solved with the modified Arnoldi algorithm as implemented in Nektar++. Linear stability of the problem is associated with the real part of the eigenvalues ω , where $\text{Re}(\omega) > 0$ represents a positive exponential growth for the corresponding eigenmode, thus an unstable mode. The imaginary part of ω is the temporal oscillation frequency for the corresponding eigenmode, and $\text{Im}(\omega) = 0$ represents a stationary mode. We have conducted additional numerical studies to verify that the computed eigenvalues are robust with respect to further mesh refinements by increasing the order of each rectangle mesh element from 4 to 8, i.e. they change by less than 0.5%. We also ran eigenvalue analysis for the 1-D Prandtl base flow using the same vertical boundary conditions, and were able to obtain the same numerical results as the separate in-house code that is described in Xiao & Senocak (2019). This provides sufficient support that the computed eigenvalues are not of a spurious nature.

3.1. Instabilities of anabatic speaker-wire vortices at 3° slope

To investigate the secondary linear instability of speaker-wire vortices, eigenvalues with the highest maximal real values for a range of streamwise wavenumbers k_x are computed for different vortex separation values b_y and stratification perturbation parameter Π_s of the base flow at the constant slope angle $\alpha = 3^\circ$. We also assume a constant Prandtl number $Pr = 0.71$ for all cases.

We observe from figure 3 that the vortex separation b_y has a profound effect on the structure of the base flow when all other flow parameters are held constant, changing both the circulation as well as vortex separation. Hence we expect that the secondary instabilities arising from these base flow vortices will also be qualitatively different depending on b_y . In total, even at constant slope angle and Prandtl number, three independent parameters determine the growth rates and oscillation frequencies of the secondary instability, which are the stratification parameter Π_s , the streamwise instability wavenumber $k_x = 2\pi/\lambda_x$, and the transverse base flow wavenumber $k_y = 2\pi/\lambda_y$, where $\lambda_y = b_y$ equals the width of the base speaker-wire vortex. In the following, we will present separately and discuss the results of the stability analysis for base speaker-wire vortices with different vortex separation values b_y . In our numerical investigations over many values for the separation b_y , we have found that the qualitative behaviour of the vortex dynamics can be classified into three categories, which can be labelled as tightly packed, intermediately packed and loosely packed.

To illustrate the nonlinear effects of different vortex instabilities, the full set of Navier–Stokes equations (2.1) and (2.2) has been solved in two as well as three dimensions using Nektar++5.0.0. The same number of spectral elements degrees of freedom as for the bi-global linear stability analysis were used to resolve the transverse yz plane, and 16 Fourier modes were used for the along-slope x direction in the 3-D simulations. The resulting animations are available as supplementary movies at <https://doi.org/10.1017/jfm.2022.508>.

3.1.1. Case I: tightly packed speaker-wire vortices

Subharmonic mode. We begin our explorations by distinguishing between the subharmonic instabilities of the base vortices (i.e. those modes whose transverse wavelength spans twice the transverse wavelength of the primary vortex instability) and the fundamental instabilities with the same transverse wavelength as the

primary mode. For speaker-wire vortices with vortex (pair) separation $b_y = 3.1$, we can see from figure 3(a) that the VPR is over 70 %. As figure 3(a) shows, the VPR decreases with increasing vortex separation b_y of the base speaker-wire vortices, which is equivalent to the primary transverse wavelength λ_y . The base flow used for modal analysis consists of two speaker-wire vortices arising from the primary linear instability mode, i.e. the transverse domain size is twice the wavelength of the primary vortex instability as described in Xiao & Senocak (2020b).

The growth rates of the most unstable secondary modes for streamwise or longitudinal wavenumbers k_x within the range $[0, 1.0]$ are shown for three different values $\Pi_s = 1.9, 2.1, 2.3$ in figure 4(a). As expected, the growth rate of any mode at a fixed streamwise wavenumber k_x grows with increasing Π_s due to an increase in the surface heat flux. It turns out that all the secondary instability modes with the largest eigenvalues have a transverse wavelength that is exactly equal to the total transverse extent of the base flow, i.e. twice the width b_y between adjacent base flow speaker-wire vortices, as can be seen in the 2-D transverse contour plot for the streamwise vorticity ω_x shown in figure 4(c), suggesting that they are indeed subharmonic instabilities. The 2-D modes have zero longitudinal wavenumbers, i.e. $k_x = 0$, and thus are constant along the streamwise direction. For the 3-D modes with $k_x > 0$, we can see from figure 4(a) that the growth rates reach a maximal value slightly exceeding the 2-D growth rate at an optimal wavenumber $k_x \approx 0.4$, and from that point on, they remain nearly constant to decrease very slowly to the 2-D growth rate at $k_x = 0$. Due to the fact that there is very little variation in growth rate as a function of the streamwise wavenumber for values less than $k_x \approx 0.4$ corresponding to the strongest mode, we can conclude that extremely long-wave or even 2-D structures that are known to appear in stably stratified channel flows (Garcia-Villalba & Del Alamo 2011) can manifest themselves when the base vortices are destabilized. All 3-D modes with positive longitudinal wavenumbers $k_x > 0$ are oscillatory with frequency increasing monotonically with growing k_x , as shown in figure 4(b). The 2-D mode with $k_x = 0$ is stationary, i.e. with zero imaginary part of its eigenvalue. At small wavenumbers k_x , the oscillation frequencies of the 3-D mode decay asymptotically to zero with decreasing k_x to converge to the stationary 2-D mode at $k_x = 0$. As figure 4(b) shows, the normalized frequencies of all three cases shown here appear to obey a simple linear dispersion relation given by $\text{Im}(\omega) = \eta k_x$, where $\eta \approx 0.327$ is determined empirically to fit all three curves. The accuracy of this fit shows that the group speed of the strongest subharmonic vortex instabilities given by $c = \partial(\text{Im}(\omega))/\partial k_x = \eta$ is nearly constant and equals η .

Existence of both 2-D and 3-D subharmonic vortex instabilities has also been identified in the study of co-rotating Stuart vortex arrays by Pierrehumbert & Widnall (1982) or as secondary instabilities in a shear layer by Corcos & Sherman (1984), where they are shown to be responsible for the merging of neighbouring vortices. Similarly, as visualized in figure 4(d), the 3-D secondary subharmonic modes of the speaker-wire vortices act by bending adjacent speaker-wire vortices in opposite directions so as to facilitate their reconnection. As shown in figure 4(e), the effect of the 2-D subharmonic mode is to strengthen one roll while weakening its sister roll within the same speaker-wire vortex, with the aim of halving the total number of vortices present within the domain. Depending on the range of permissible streamwise wavelength, which itself depends on the length of the domain, the strongest subharmonic mode is either purely 2-D or 3-D. When the streamwise domain length is L_x , a mode with wavenumber within $2\pi/L_x$ of the optimal wavenumber k_O will manifest itself. Thus, for large values of L_x , a 3-D mode with wavelength close to the optimal wavelength will be favoured; however, in the case when

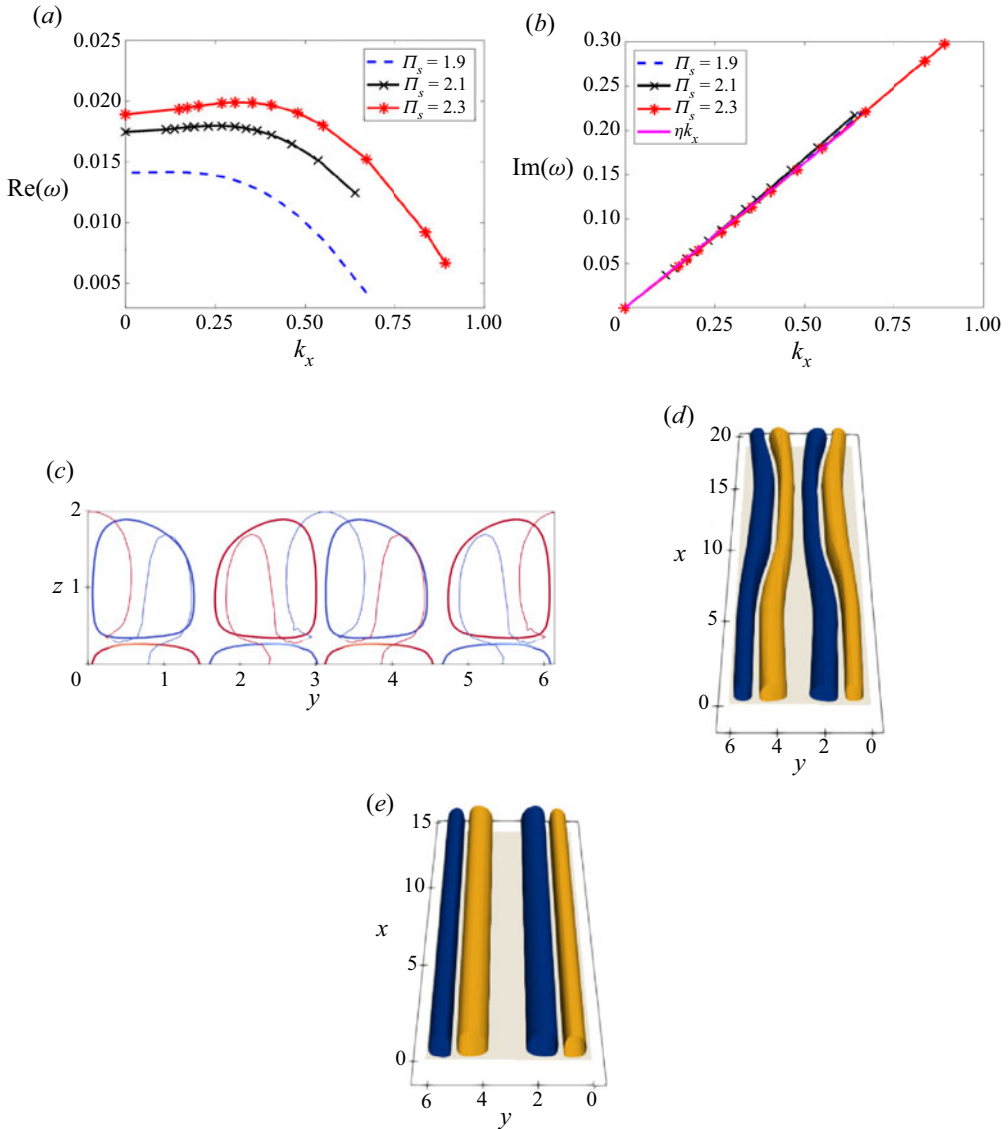


Figure 4. Characteristics of the subharmonic mode for tightly packed speaker-wire vortices at different values of Π_s as a function of the longitudinal wavenumber $k_x = 2\pi/\lambda_x$: (a) growth rate $\text{Re}(\omega)$; (b) oscillation frequency $\text{Im}(\omega)$, along with the linear dispersion relation $\text{Im}(\omega) = \eta k_x$ ($\eta \approx 0.327$). (c) Contours of streamwise vorticity for the instability mode (thin lines) at $\Pi_s = 1.9$ on the yz plane in relation to the base flow (thick lines). (d) Streamwise vorticity contours of base speaker-wire vortices perturbed by 3-D subharmonic instability at $\Pi_s = 2.3$. (e) Streamwise vorticity contours of base speaker-wire vortices perturbed by 2-D subharmonic instability. All shown contours are at 5% of the maximal vorticity magnitude. Video of the evolution of the 2-D subharmonic instability for tightly-packed vortices is available as supplementary movie 1.

the streamwise domain length is less than $2\pi k_0$, the 2-D subharmonic mode will come out the strongest.

Fundamental mode. The fundamental secondary instability has, by definition, a transverse wavelength equalling the transverse wavelength λ_y of the primary instability, or one-half of the wavelength of a subharmonic mode. Thus the base flow used in the

present analysis consists of only one single speaker-wire vortex that rises from the primary linear instability mode in order to ensure that the maximal transverse wavelength λ_y of the eigenmodes computed here cannot exceed the transverse wavelength of the primary vortex instability.

The growth rates and oscillation frequencies of the most unstable modes for streamwise wavenumbers k_x within the range $[0, 1.0]$ are shown for three different values $\Pi_s = 2.9, 3.0, 3.05$ in figures 5(a) and 5(b). As shown in figure 5(c), the transverse wavelength of the fundamental mode is approximately 3, thus equal to the base vortex separation b_y . Compared with the subharmonic mode that we discussed previously and visualized in figure 4(a), the growth rates of these fundamental modes are around five times smaller despite possessing larger normalized surface fluxes, which is also indicated by the larger Π_s values in their base flows. At the lower values of Π_s , as displayed for the subharmonic modes in figure 4(a), there exist no unstable fundamental modes. This signifies that there is a clear separation between the fundamental and subharmonic modes, and that the fundamental modes are inherently weaker than their subharmonic counterparts, whose transverse wavelength is twice as large. The flow-physical implication of this clear gap between the subharmonic and fundamental modes is that the most dominant vortex dynamics is the merger or reconnection of two adjacent speaker-wire vortices involving four rolls in total, rather than reconnection within a single vortex pair.

Figure 5(a) shows that with increasing normalized surface heat flux Π_s , the growth rate of the strongest mode at the large as well as smallest streamwise wavenumbers k_x also grows. However, for intermediate wavenumber values $0.05 < k_x < 0.2$, the growth rates are higher for lower Π_s . Similar to what we have observed in the case of subharmonic modes, there exist stationary 2-D fundamental modes that do not vary along the streamwise along-slope direction; their growth rates are shown in figure 5(a) as the values at the wavenumber $k_x = 0$. In contrast to the subharmonic modes, the strongest 3-D fundamental modes ($k_x > 0$) have lower growth rates than their 2-D counterparts for all values of k_x .

All the 3-D fundamental modes are oscillatory, and their frequencies increase monotonically with the streamwise wavenumber k_x , as shown in figure 5(b). At small wavenumbers k_x , the frequency of the 3-D fundamental mode decays asymptotically to zero to become the stationary 2-D mode at $k_x = 0$. It can be seen that for larger wavenumbers with $k_x > 0.35$, the normalized frequencies of the strongest fundamental modes at the three values for Π_s shown here fit approximately a simple linear dispersion relation given by $\text{Im}(\omega) = \zeta k_x$, where $\zeta \approx 0.25$ is determined empirically to fit all three curves. At lower wavenumbers $k_x < 0.2$, the fundamental mode from another branch of the spectrum with higher frequency becomes stronger than the dominant mode at larger wavenumbers, which manifests itself in an abrupt jump of the oscillation frequency $\text{Im}(\omega)$ of the strongest fundamental mode as a function of k_x , as shown in figure 5(b).

Fundamental instabilities of longitudinal rolls, i.e. modes that have the same transverse wavelength as the base vortices, have been studied extensively in previous works as well. The most prominent representative of such a mode is the Crow instability for a pair of vortices suspended in unstratified air (Crow 1970). Fundamental modes have also been identified as instabilities of Rayleigh–Bénard convection rolls, which aim to distort the structure and spacing of the rolls to bring them closer to the optimal wavelength (Clever & Busse 1974). More recently, fundamental vortex instabilities have also been found in strongly stratified fluids such as the so-called zig-zag instability studied in Billant (2010). Similar to the fundamental vortex instabilities discovered in Pierrehumbert &

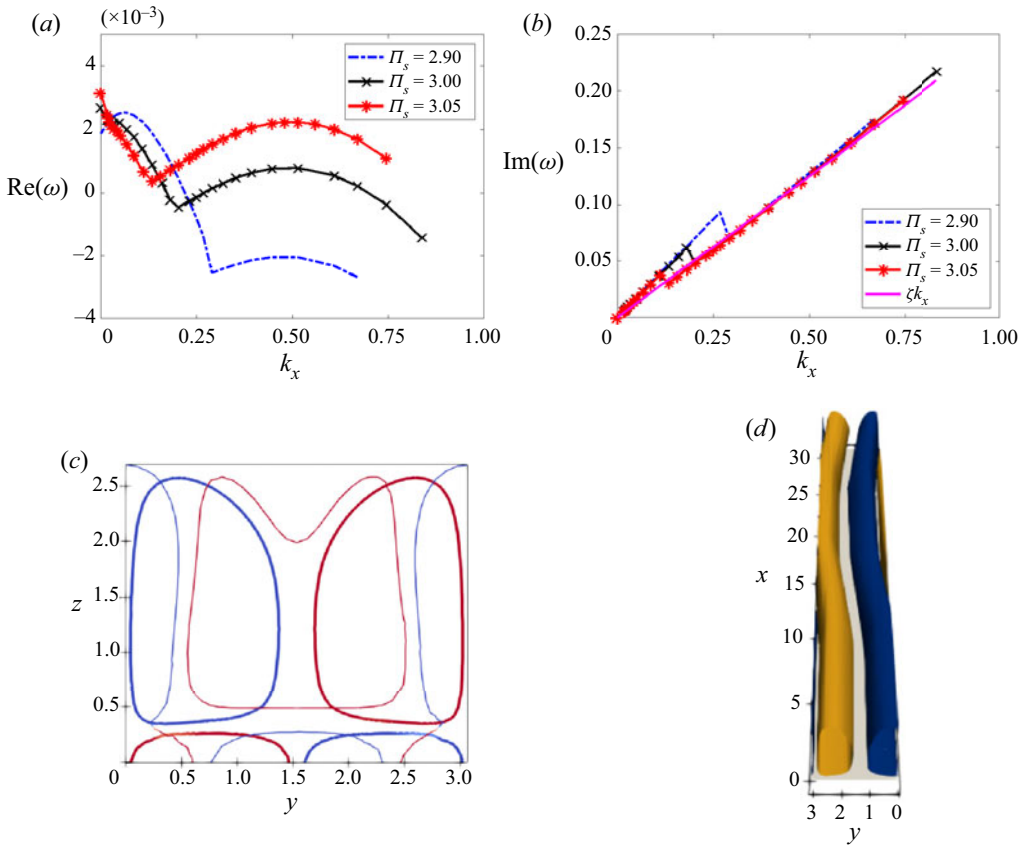


Figure 5. Characteristics of the fundamental mode for tightly packed speaker-wire vortices at different values of Π_s as a function of the longitudinal wavenumber k_x : (a) growth rate $\text{Re}(\omega)$; (b) oscillation frequency $\text{Im}(\omega)$, along with the linear dispersion relation $\text{Im}(\omega) = \zeta k_x$ ($\zeta \approx 0.25$). (c) Streamwise vorticity contours of two adjacent rolls from neighbouring speaker-wire vortices at $\Pi_s = 3.05$ on the transverse y - z plane. (d) Streamwise vorticity contours of base speaker-wire vortices perturbed by the fundamental instability at $\Pi_s = 3.05$. All contours are displayed at 5% of the maximal vorticity magnitude.

Widnall (1982), we expect that the main effect of the fundamental modes is to cause parallel displacement and symmetric distortion of all vortices. As visualized in figure 5(d), the 3-D fundamental mode causes sinusoidal bending and distortion of each speaker-wire vortex. However, unlike the well-known symmetric Crow instability (Crow 1970), which bends two sister rolls towards each other to facilitate their connection, the fundamental mode for speaker-wire vortices can only bend both vortices within a pair along the same direction, as shown in figure 5(d).

Coherent nature of single speaker-wire vortex. We observe from figures 4(d) and 5(d), in both subharmonic and fundamental modes, that the two rolls within the same speaker-wire vortex always bend in the same direction, thus preventing a vortex reconnection or merger. This means that a single pair of vortices can remain in its basic pair structure even after the initial onset of instabilities, thus justifying their designation as a unique coherent vortex structure. Similar vortex structures that remain stable and coherent over large wavelengths have been observed in the Langmuir vortices on the surface of seas and oceans, as described in Craik & Leibovich (1976).

3.1.2. *Case II: intermediately packed speaker-wire vortices*

Subharmonic and fundamental modes. For a larger speaker-wire vortex separation $b_y = 4.1$, we observe from [figure 3](#) that the VPR of speaker-wire vortices is decreasing to around 60%. This indicates that relative to the previous vortex configuration (i.e. Case I) with a smaller transverse vortex wavelength, the two speaker-wire vortices move tighter towards each other after reaching the end of their linear growth phase, leading to a clearer separation of adjacent speaker-wire vortices.

To uncover both subharmonic and fundamental instabilities of the base speaker-wire vortices, we used two sets of base flows for modal analysis, consisting of two pairs and one pair of speaker-wire vortices arising from the primary linear instability mode, respectively. The growth rates of the most unstable secondary modes for streamwise wavenumbers k_x within the range $[0, 0.8]$ are shown for three different values $\Pi_s = 2.25, 2.4, 2.5$ in [figure 6\(a\)](#). In contrast to the previous configuration (Case I) with closely spaced speaker-wire vortices, there are no unstable 2-D modes, i.e. modes with a positive growth rate at $k_x = 0$. As expected, the maximal growth rate of the secondary instability is larger for the higher value $\Pi_s = 2.4$ than for the smaller value $\Pi_s = 2.25$, and the optimal streamwise wavenumber with maximal growth is also larger for $\Pi_s = 2.4$. [Figure 6\(a\)](#) also shows that the subharmonic mode for $\Pi_s = 2.25$ attains its maximal growth rate at a larger streamwise wavenumber, $k_x \approx 0.4$, than its fundamental counterpart, which is strongest at the wavenumber $k_x \approx 0.1$, hence the unstable subharmonic modes tend to have a clearly smaller streamwise wavelength than the fundamental ones.

A comparison between subharmonic and fundamental modes at the same value $\Pi_s = 2.25$ also shows that in contrast to the base configuration with smaller vortex separation as described above, the subharmonic mode does not achieve a larger maximal growth rate than its fundamental counterpart. This implies that in contrast to the previous base vortex configuration with a smaller vortex separation b_y , the fundamental instability is of equal importance to the subharmonic mode. Thus, in addition to the merger between neighbouring speaker-wire vortices due to the subharmonic mode, we would also expect to see the effect of the fundamental mode during flow transition, which could be a parallel translation of all vortices or (anti-)symmetric bending of sister rolls as described by Pierrehumbert & Widnall (1982) and Corcos & Sherman (1984). Due to symmetry, this transverse translation is equally likely to move along the positive or negative y direction, depending on the nature of the initial disturbance.

We observe from [figure 6\(b\)](#) that the normalized frequencies of the most dominant subharmonic modes at the three values for Π_s shown here appear to fit a linear dispersion relation given by $\text{Im}(\omega) = \eta k_x$, where $\eta \approx 0.124$ is determined empirically to match approximately all three curves. The accuracy of this linear relation demonstrates that the group speed of the strongest subharmonic vortex instabilities given by $c = \partial(\text{Im}(\omega))/\partial k_x = \eta$ is nearly constant and equals η . It should be noticed that this value for $\eta \approx 0.124$ is roughly three times as small as its value for Case I with $\eta \approx 0.327$. This means that the subharmonic instability waves travel far more slowly on base vortices with an intermediate vortex separation than on more closely packed speaker-wire vortices.

As shown in [figure 6\(c\)](#), the transverse wavelength of the subharmonic mode is approximately the transverse domain length, hence twice the base speaker-wire vortex separation b_y . [Figure 6\(d\)](#) shows that 3-D secondary subharmonic modes bend both sister rolls within the same speaker-wire vortex in the same direction, but pull neighbouring rolls in adjacent speaker-wire vortices in opposite directions. Thus the reconnection and merger between rolls from different speaker-wire vortices is facilitated over a merger within a single speaker-wire vortex.

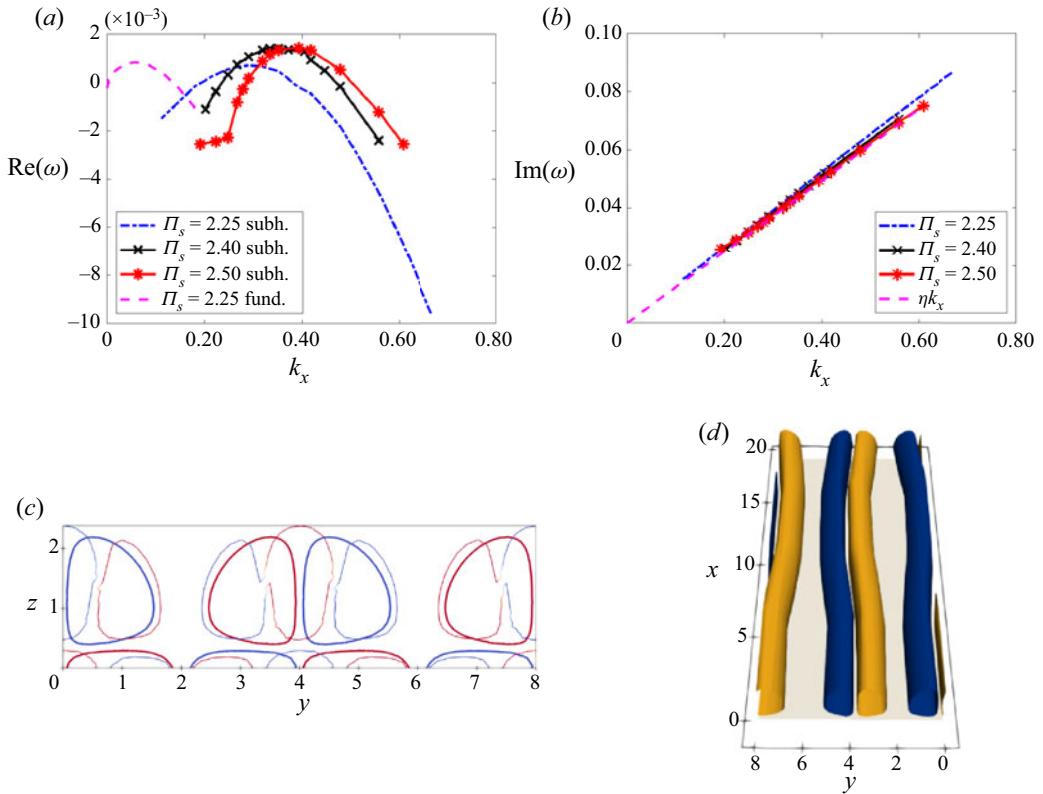


Figure 6. Characteristics of the subharmonic mode for intermediately packed speaker-wire vortices at different values $\Pi_s = 2.25, 2.4, 2.5$ as a function of the longitudinal wavenumber k_x : (a) growth rates $\text{Re}(\omega)$ of 3-D modes, along with the fundamental mode at $\Pi_s = 2.4$ for comparison; (b) oscillation frequency $\text{Im}(\omega)$, along with the linear dispersion relation ηk_x ($\eta \approx 0.124$). (c) Contours on the transverse yz plane of streamwise vorticity for the 3-D subharmonic instability (thin lines) at $\Pi_s = 2.4$ in relation to the base flow (thick lines). (d) Streamwise vorticity contours of base speaker-wire vortices perturbed by the subharmonic instability at $\Pi_s = 2.4$. All contours are shown at 5% of the maximal vorticity magnitude.

The growth rates and oscillation frequencies of the strongest fundamental modes on base vortices with intermediate vortex separation are displayed in figures 7(a) and 7(b). They confirm the previous observation that the fundamental instability is a long-wave mode, which attains its maximum growth rate at wave streamwise numbers $k_x < 0.1$ compared to the optimal frequency of the subharmonic mode at around $k_x \approx 0.4$. Figure 7(b) shows that the oscillation frequencies of the most dominant fundamental modes at the three different values for Π_s shown here seem to follow the linear dispersion relation given by $\text{Im}(\omega) = \zeta k_x$, with $\zeta \approx 0.142$ being slightly larger than the value $\eta \approx 0.124$ for the subharmonic modes. This value $\eta \approx 0.124$ is roughly one-half of its value at the lesser base vortex separation discussed above with $\eta \approx 0.25$, which indicates that the fundamental modes travel half as fast on base vortices with an intermediate vortex separation than on more densely packed base vortices.

As figure 7(c) shows, the transverse wavelength of the fundamental mode is approximately 4 and equals the base speaker-wire vortex separation b_y . Figure 7(d) indicates that the 3-D fundamental mode bends all rolls within a speaker-wire vortex in the same direction. Thus the mode cannot generate a merger or reconnection of the two rolls

Speaker-wire vortices in stratified anabatic slope flows

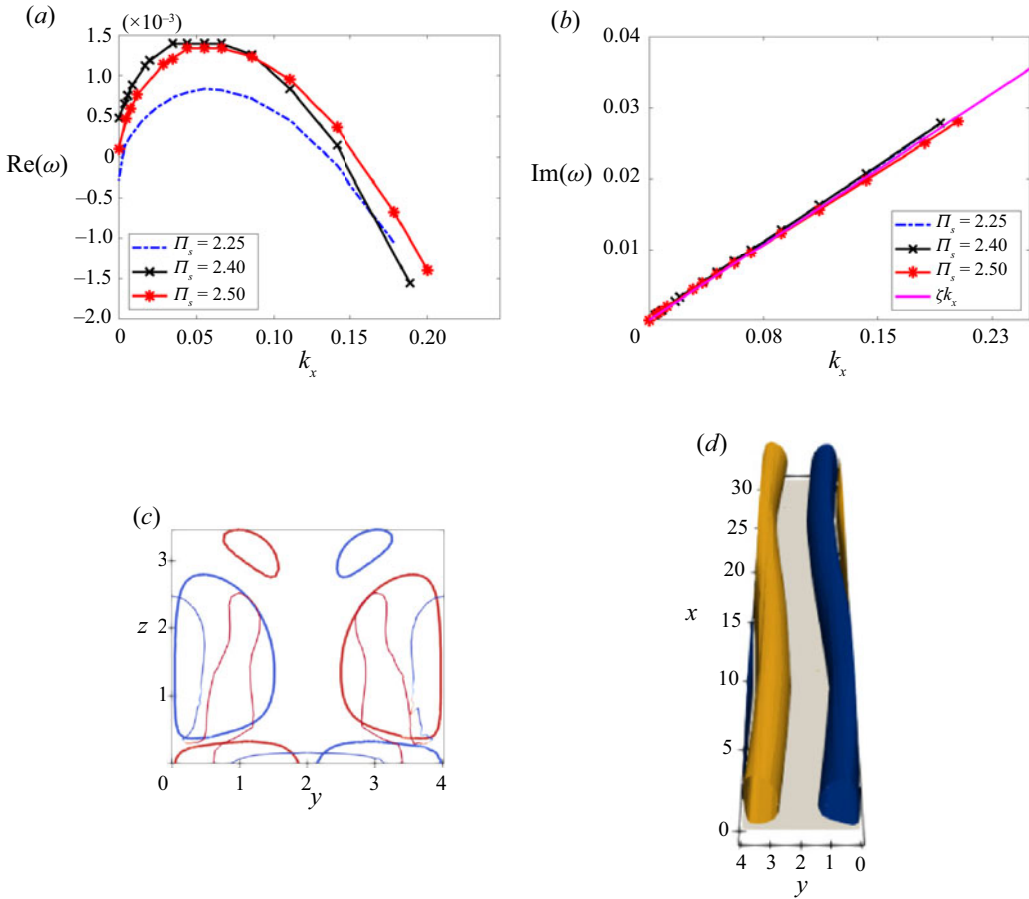


Figure 7. Characteristics of the fundamental mode for intermediately packed speaker-wire vortices at different values of Π_s as a function of the longitudinal wavenumber k_x : (a) growth rate $\text{Re}(\omega)$; (b) oscillation frequency $\text{Im}(\omega)$, along with the linear relation ζk_x ($\zeta = 0.142$). (c) Streamwise vorticity contours of two adjacent rolls from neighbouring speaker-wire vortices on the transverse plane for the 3-D fundamental instability at $\Pi_s = 2.4$. (d) Streamwise vorticity contours of two rolls from neighbouring speaker-wire vortices perturbed by the fundamental instability at $\Pi_s = 2.4$. All shown contours are at 5% of the maximal vorticity magnitude.

within a single speaker-wire vortex. The effect of the 2-D fundamental mode is to cause a parallel translation of all rolls similar to fundamental Stuart vortex instabilities described in Pierrehumbert & Widnall (1982), and will not be displayed explicitly here.

3.1.3. Case III: loosely packed speaker-wire vortices

Subharmonic and fundamental modes. For an even larger speaker-wire vortex separation $b_y = 5.0$, figure 3(a) shows that the VPR decreases further, to around 50%. This indicates that beyond the linear growth phase of the primary instability, the respective centres of the two vortices within each speaker-wire pair are moving further towards each other such that the width of each speaker-wire vortex is smaller than one-half of the distance b_y between adjacent speaker-wire vortices. The implication of this tightening of each speaker-wire vortex is that there is now sufficient space between two pairs to fit in an additional speaker-wire vortex.

To compute subharmonic and fundamental instabilities for this base speaker-wire vortex configuration, we used two sets of base flows for modal analysis: two speaker-wire vortices for the subharmonic mode and one single pair for the fundamental mode, all with the pair spacing $b_y = 5.0$. The growth rates of the most unstable secondary modes for streamwise wavenumbers k_x within $[0, 0.8]$ are shown for different values $\Pi_s = 2.2, 2.3, 2.4$ in [figure 8\(a\)](#), which indicates that the most dominant modes are subharmonic. As for the other cases, the maximal growth rate of the secondary instability is larger for the higher value $\Pi_s = 2.4$ than for the smaller value $\Pi_s = 2.3$, and the optimal streamwise wavenumber k_x with maximal growth rate is also larger for $\Pi_s = 2.4$ than for $\Pi_s = 2.3$.

Comparison with the growth rate of the 3-D fundamental mode at $\Pi_s = 2.4$ in [figure 8\(a\)](#) shows that the subharmonic mode at the same Π_s value achieves a clearly larger growth rate for all streamwise wavenumbers k_x . This assertion is supported further when we compare the growth rates for fundamental modes at $\Pi_s = 2.35, 2.4, 2.45$ shown in [figure 9\(a\)](#) against the growth rates shown in [figure 8\(a\)](#) for subharmonic modes. This means that similar to Case I with the smallest vortex separation ($b_y = 3.1$), but in contrast to Case II with an intermediate spacing of the speaker-wire vortices ($b_y = 4.1$), there exists a gap between the subharmonic and fundamental modes when all other base flow parameters are the same. Thus we would expect to see the dominant effect of the subharmonic mode at $\Pi_s \approx 2.4$ during flow transition. However, as will be shown later, this behaviour can change at larger Π_s values.

The oscillation frequencies of the strongest subharmonic modes for base vortices with large vortex separation are displayed in [figure 8\(b\)](#), showing that the frequencies of the most dominant fundamental modes at the three different values for Π_s displayed here appear to fit a linear dispersion relation given by $\text{Im}(\omega) = \kappa + \eta k_x$ with $\kappa \approx 0.014$, $\eta \approx 0.32$. This shows that in contrast to the previous configurations with smaller base vortex separations, even the 2-D subharmonic instability ($k_x = 0$) is oscillatory with frequency κ . The group velocity η for the subharmonic modes is approximately the same as the corresponding value for subharmonic modes at small base vortex separation, which is $\eta \approx 0.327$, clearly larger than the value at intermediate base vortex separation.

As shown in [figure 8\(c\)](#), the transverse wavelength of the subharmonic mode is approximately 10, hence twice the value of the base speaker-wire vortex separation b_y . [Figure 8\(d\)](#) shows that 3-D subharmonic modes bend both sister rolls within the same speaker-wire vortex in the same direction, but pull neighbouring rolls in adjacent speaker-wire vortices in opposite directions. Thus the reconnection and merger between rolls from different speaker-wire vortices is facilitated over a merger within a single speaker-wire vortex. The effect of the 2-D subharmonic mode is displayed in [figure 8\(e\)](#): it can be seen that one pair of neighbouring speaker-wire vortices moves closer towards each other in the precursor to a merger, while at the same time distancing themselves from their other neighbours and increasing the in-between space where additional vortices can be formed. This can be seen in the animations of the evolution of subharmonic instabilities obtained via numerical integration of the 3-D Navier–Stokes equations (2.1) and (2.2), available as supplementary movies 2 and 3.

As displayed in the movies, the nonlinear dynamics subharmonic instability for well-separated base vortices is different to a mere merger that occurs for vortices that are more closely packed. As predicted by linear stability analysis, the subharmonic mode manifests itself initially by bending neighbouring pairs in opposite directions. However, at later times, novel vortices emerge in the free space between the pairs, and those newly created vortices will merge later with one of the original base vortices. When the spacing

Speaker-wire vortices in stratified anabatic slope flows

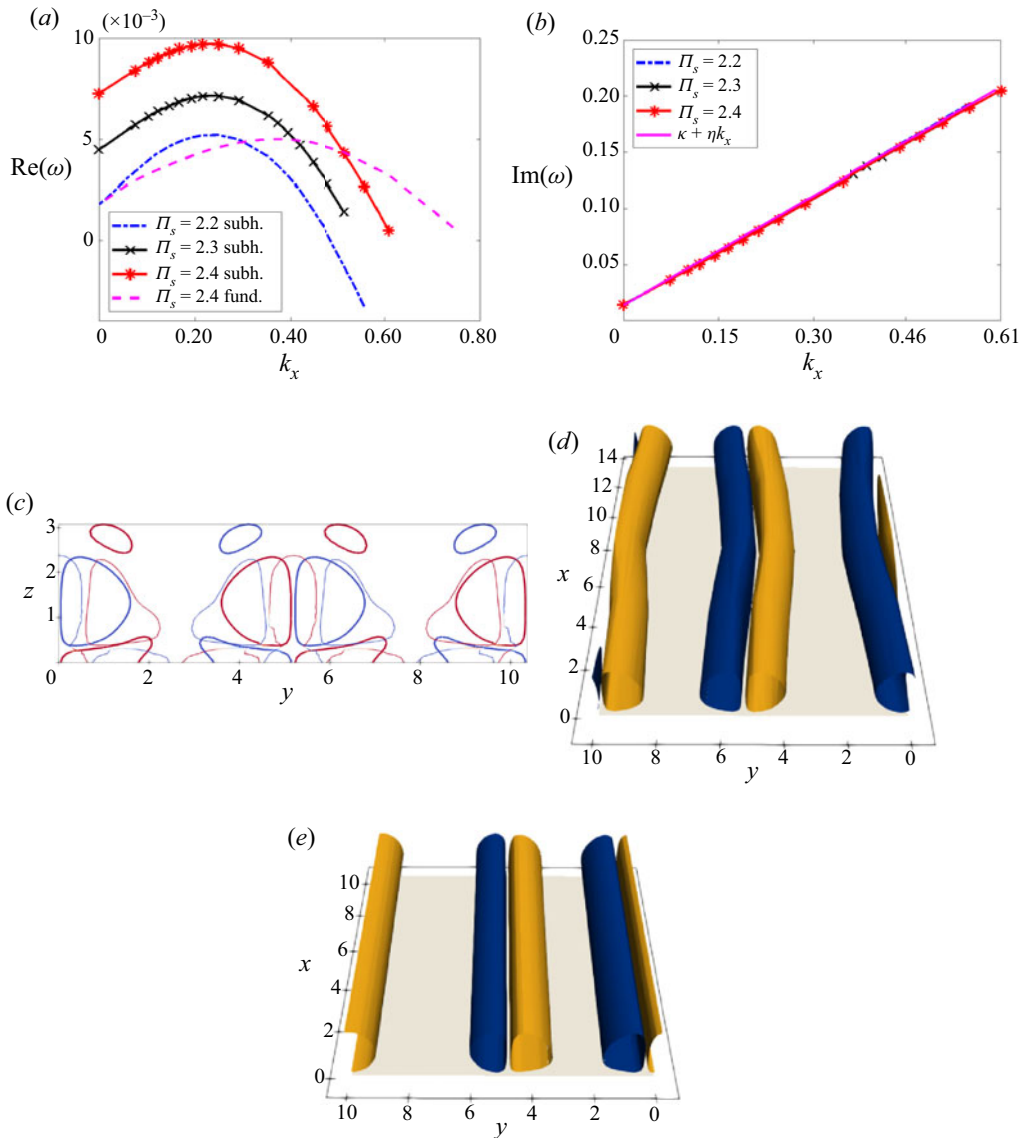


Figure 8. Characteristics of the subharmonic mode for loosely packed speaker-wire vortices at different values of Π_s as a function of the longitudinal wavenumber k_x : (a) growth rate $\text{Re}(\omega)$; (b) oscillation frequency $\text{Im}(\omega)$, along with the linear relation $\kappa + \eta k_x$ ($\kappa = 0.014$, $\eta = 0.32$). (c) Contours of streamwise vorticity on the transverse plane for the subharmonic instability mode (thin lines) at $\Pi_s = 2.4$ in relation to the base flow (thick lines). (d) Streamwise vorticity contours of base speaker-wire vortices perturbed by the subharmonic instability at $\Pi_s = 2.4$. (e) Streamwise vorticity contours of base speaker-wire vortices perturbed by 2-D subharmonic instability. Videos of the evolution of the 3-D and 2-D subharmonic instabilities for the loosely packed vortices are available in supplementary movies 2 and 3. All contours are displayed at 5% of the maximal vorticity magnitude.

between base vortices is small, then this phenomenon of vortex creation cannot occur due to the lack of free spacing, hence the only dynamics is the merger of adjacent speaker-wire vortices. This supports our main message that the vortex instability dynamics is strongly dependent on the spacing between adjacent pairs, which is quantified by the vortex packing

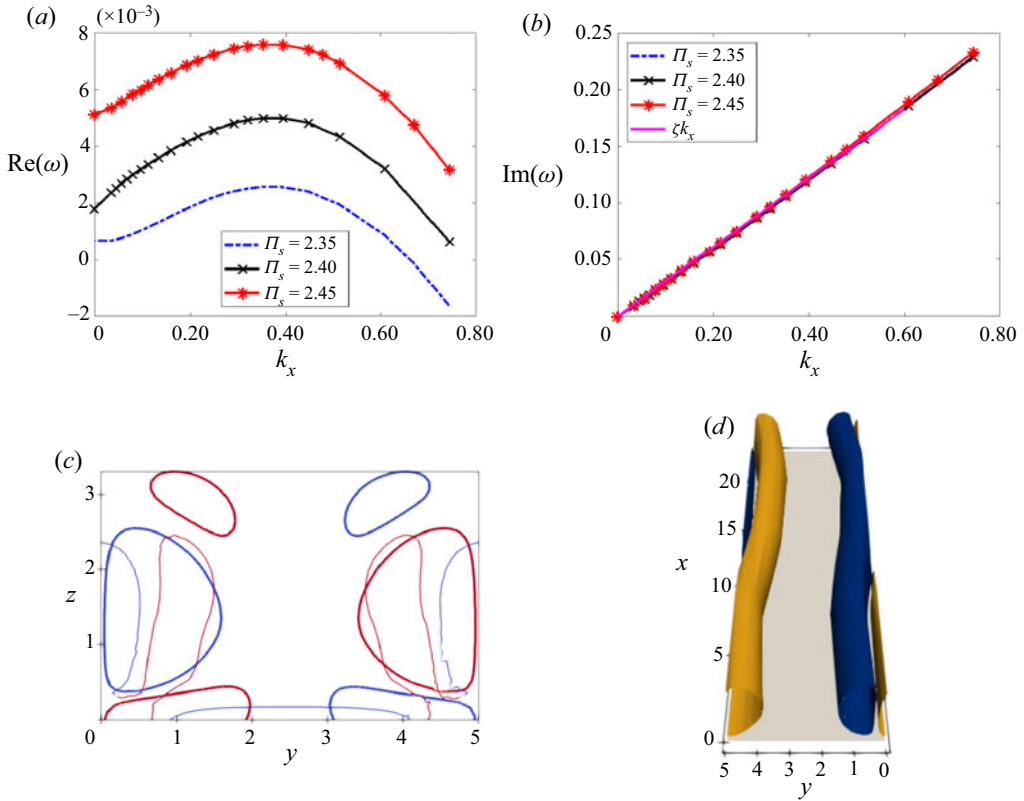


Figure 9. Characteristics of the fundamental mode for loosely packed speaker-wire vortices at different values of Π_s as a function of the longitudinal wavenumber k_x : (a) growth rate $\text{Re}(\omega)$; (b) oscillation frequency $\text{Im}(\omega)$ and the linear dispersion relation $\text{Im}(\omega) = \zeta k_x$ ($\zeta = 0.305$). (c) Streamwise vorticity contours of two adjacent rolls from neighbouring speaker-wire vortices on the transverse yz plane for the fundamental instability (thin lines) at $\Pi_s = 2.4$. (d) Streamwise vorticity contours of base speaker-wire vortices perturbed by the fundamental instability at $\Pi_s = 2.4$. Videos of the evolution of the 3-D and 2-D fundamental instabilities for the loosely packed vortices are available in supplementary movies 4 and 5. All contours are shown at 5% of the maximal vorticity magnitude.

ratio (VPR) introduced above. However, linear stability analysis by itself can only predict the initial onset of vortex instability, and the subsequent nonlinear evolution of the vortices is shown in the supplementary movies.

The growth rates and oscillation frequencies for the strongest fundamental modes on loosely packed base vortices with large vortex separation are displayed in figures 9(a) and 9(b). In contrast to base vortices with intermediate vortex separation discussed above, the fundamental instability attains its maximum growth rate at higher wave streamwise numbers $k_x \approx 0.4$ compared to the most dangerous frequency of the subharmonic mode at around $k_x \approx 0.2$. As shown in figure 9(b), the frequencies of the strongest fundamental modes at the three different values for Π_s displayed here follow closely the linear dispersion relation given by $\text{Im}(\omega) = \zeta k_x$ with $\zeta \approx 0.305$, which is only slightly smaller than the value $\eta \approx 0.32$ for the subharmonic modes. This would indicate that the fundamental modes travel at around the same speed as their subharmonic counterparts.

As displayed in figure 9(c), the transverse wavelength of the fundamental mode is approximately 5, which equals the base speaker-wire vortex separation b_y . Figure 9(d)

indicates that 3-D fundamental instabilities bend all rolls within speaker-wire vortices along the same direction. Thus by themselves they cannot generate the dynamics for merger within a single speaker-wire vortex. The effect of the 2-D fundamental mode is to cause a parallel translation of all rolls similarly as fundamental Stuart vortex instabilities described in Pierrehumbert & Widnall (1982), and will not be displayed explicitly here.

3.2. *Effect of speaker-wire vortex spacing on instability*

As we have seen from the previous presentations of instabilities for different speaker-wire vortex configurations, the distance b_y between adjacent speaker-wire vortices is crucial in determining which kind of modes are favoured to destabilize the vortices. For both small and large values of b_y , our prior analysis suggests that subharmonic modes, i.e. those with transverse wavelength $\lambda_y = 2b_y$, are clearly stronger than their fundamental counterparts with half the wavelength $\lambda_y = b_y$. However, when b_y takes on an intermediate value, both fundamental and subharmonic modes may have similar growth rates at smaller stratification numbers Π_s .

To investigate the influence of vortex separation b_y on secondary instability properties in a more systematic way, we have prepared a series of base flows containing speaker-wire vortices with vortex separation b_y within the range [3.0, 5.2] and computed their most unstable subharmonic as well as fundamental modes. For the study of subharmonic modes, we chose the stratification number $\Pi_s = 1.9$ for all base flow configurations that differ only by their vortex separation b_y . The growth rates and oscillation frequencies of the most unstable 3-D subharmonic modes with different streamwise wavenumbers $k_x = 0.22, 0.33, 0.44$ as a function of b_y are shown in figures 10(a) and 10(b). These results corroborate our earlier observations about the dependence of the subharmonic mode on vortex separation b_y : the subharmonic instability assumes its strongest growth rate when b_y is the smallest, and becomes weaker when b_y is increased until reaching its minimum, which is negative, at an intermediate value $b_y \approx 4.2$. From that point onwards, the subharmonic instability starts to get stronger again with further increases in b_y ; however, at the largest $b_y = 5.1$ shown here, even though again at a positive growth rate, it never regains its peak strength at the smallest vortex separation $b_y = 3.1$. Figure 10(b) shows that in contrast to the growth rate, the oscillation frequency of the strongest subharmonic mode at a given wavenumber k_x generally grows monotonically with vortex separation b_y for all $b_y \leq 4.5$. For larger vortex separation values b_y , the oscillation frequency stagnates visibly at its value for the vortex separation $b_y = 4.5$.

To study the fundamental instability modes, we have chosen the stratification number $\Pi_s = 2.85$ for all base flow configurations. The growth rates and oscillation frequencies of the most unstable 3-D fundamental modes at three different streamwise wavenumbers $k_x = 0.41, 0.66, 0.84$ as a function of b_y are shown in figures 11(a) and 11(b). These results show that in contrast to the subharmonic modes, the fundamental instability increases in strength with growing vortex separation b_y , starting with negative growth rates at $b_y = 3.1$, and becoming positive for $b_y > 4.0$. A physical explanation for this could be that at larger distances between adjacent speaker-wire vortices, the influence between vortices within a pair outweighs the effect of the more distant vortices at a different vortex pair. Figure 11(b) shows that the oscillation frequency of the strongest fundamental mode also grows with increasing b_y throughout the entire range as displayed here.

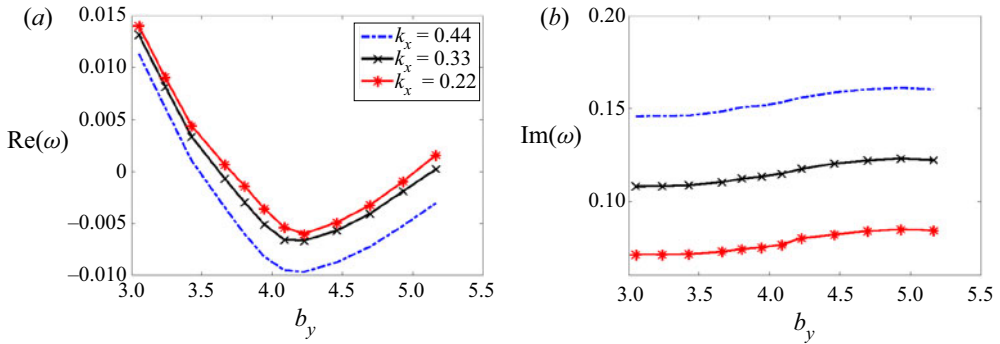


Figure 10. Characteristics of the subharmonic secondary instability for different streamwise wavenumbers k_x at $\Pi_s = 1.9$ as a function of the vortex separation b_y (which is also the transverse wavelength of the base vortices): (a) growth rate; (b) oscillation frequency.

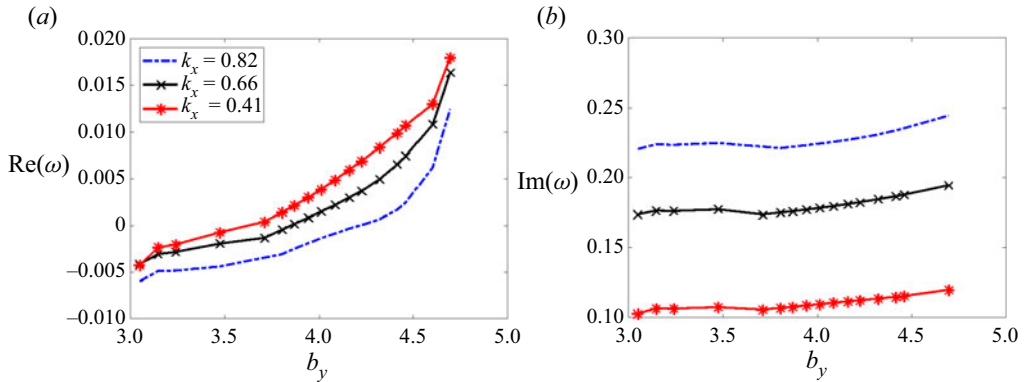


Figure 11. Characteristics of the fundamental secondary instability for different streamwise wavenumbers k_x at $\Pi_s = 2.85$ as a function of the base vortex separation b_y : (a) growth rate compared to primary linear instability; (b) oscillation frequency.

4. Conclusions

We have carried out a linear bi-global stability analysis for stationary longitudinal rolls that emerge as a primary instability from the laminar 1-D anabatic Prandtl slope flow at low angles. We have identified the pair of counter-rotating rolls as unique flow structures, and designated them as speaker-wire vortices. Despite the apparent resemblance of the longitudinal rolls in our study to other well-known counter-rotating vortex pairs reported in the literature, our base flow configuration has multiple distinctly unique features. First, it includes an independent background stratification that is at an oblique angle to the heated solid slope surface. Second, the rolls in our base flow configuration have three non-zero velocity components even though the flow field itself has zero gradient along the streamwise direction. As a result, it is not surprising that the instability dynamics of these speaker-wire vortices are also distinct from the hitherto known vortex pair instabilities.

Our results for secondary instabilities of speaker-wire vortices have shown that the vortex packing ratio (VPR), or equivalently, the vortex separation b_y , i.e. the distance between two adjacent speaker-wire vortices, plays a major role in determining which stability mode is the most significant in destabilizing the vortices under anabatic slope flow conditions. The growth rate of the most dominant subharmonic mode as a function

of vortex spacing b_y has a parabola-like shape: it is maximal at the lowest values $b_y \leq 3.1$, then gradually decreases to its minimum at $b_y \approx 4.4$ when the base vortex configuration is the most stable, but starts increasing again for larger b_y . In contrast, the growth rate of the strongest fundamental mode increases with larger vortex separation b_y . For closely-packed as well as sparsely-packed vortex configurations, i.e. those with VPR over 70 % or less than 50 %, the subharmonic secondary instability is far more dominant than the fundamental modes, which become unstable only at higher normalized surface heat flux values. On the other hand, when the VPR drops to 60 % at an intermediate vortex separation $b_y \approx 4.1$, the long-wave fundamental mode may become roughly equal to the strongest subharmonic mode. For all the subharmonic and fundamental instability modes computed for speaker-wire vortices of different VPR and vortex separation values, we have found that rolls within the same speaker-wire vortex always bend in the same direction, hence keeping the same distance towards each other even after being destabilized. The implication of this dynamic is that in speaker-wire vortices, reconnections are possible only when at least two speaker-wire vortices (i.e. four vortex rolls) are present, whereas two rolls within a single speaker-wire vortex are unlikely to reconnect with each other even after the onset of instabilities. This dynamic is in contrast to most other well-known vortex instabilities such as the Crow instability, the elliptic instability or the zig-zag instability, which has led us to identify the speaker-wire vortex as a novel coherent vortex unit.

The subharmonic and fundamental modes in speaker-wire vortices come in both 3-D and 2-D types. The 2-D subharmonic mode for closely packed base vortex configurations acts to weaken every second vortex, eventually destroying them and freeing up vortex-free space between the remaining rolls. On the other hand, for sparsely-packed base vortex configurations, the 2-D subharmonic mode moves two adjacent speaker-wire vortices closer towards each other as a precursor to a vortex merger, which simultaneously creates additional space between two other vortices in which additional vortices can be formed, resulting in a more densely packed vortex array. The physical interpretation of this dynamic would be that these 2-D instabilities aim at generating a vortex configuration that has an optimal intermediate distance between the speaker-wire vortices, and is neither too densely nor too sparsely packed. The 2-D fundamental mode, which can play a meaningful role at an intermediate base vortex distance $b_y \approx 4.1$ only by not being dominated by its subharmonic counterpart, has the net effect of displacing all base speaker-wire vortices along the transverse direction at the same speed.

The 3-D secondary instability modes, i.e. those that vary along the streamwise or equivalently the along-slope direction, have been shown to cause streamwise sinusoidal bending of each vortex in the base configuration. The 3-D subharmonic mode, whose transverse wavelength is twice the base vortex separation, moves two adjacent speaker-wire vortices closer to each other, and also bends the two neighbouring rolls belonging to different speaker-wire vortices along opposite directions. As a result, the segments on each roll that are bent towards their neighbour from the adjacent speaker-wire vortex have the smallest distance to the corresponding segment in its neighbouring vortex, eventually getting close enough to become sites of a vortex reconnection and thus ripped from its sister roll in the original speaker-wire vortex. For tightly packed base vortex configurations, the growth rates of 3-D subharmonic modes remain nearly constant for all streamwise wavenumbers smaller than that of the most dominant mode, thus revealing the presence of potential long-wave instabilities. The 3-D fundamental mode, with a transverse wavelength equivalent to the vortex separation of the base speaker-wire vortices, bends all rolls in all speaker-wire vortices along the same direction, thus the distances between them remain the same as in the original base configuration before the onset of instability.

Thus the fundamental mode by itself cannot be the mechanism leading to vortex reconnection. Instead, after a sufficiently long time, the subharmonic instability will eventually manifest itself by either moving two neighbouring speaker-wire vortices towards each other (densely packed case) or creating new vortices between two pairs (thinly packed case), resulting in the reconnection between two adjacent rolls that are not from the same speaker-wire vortex as in the base configuration as described above.

One of the most poignant findings uncovered in our study is that for all fundamental and subharmonic speaker-wire vortex instabilities, the sister rolls within a single speaker-wire vortex always bend in the same direction, thus keeping the distance from each other and preventing reconnection between them.

This implies that the only possible vortex reconnection dynamics under Prandtl's anabatic slope flow model requires four vortex rolls in two speaker-wire vortices, whereas one single speaker-wire vortex is able to maintain its two-roll structure even after the onset of vortex instabilities. The sensitivity of vortex dynamics with respect to the base vortex separation, which characterizes the degree of vortex array density along the transverse direction, is also a distinct feature not observed in other secondary instabilities such as those occurring in convective boundary layers. Hence the speaker-wire vortex system described in this work merits its designation as a novel coherent flow structure whose dynamics may have profound impact on turbulent transitions in stably stratified boundary layers.

Supplementary movies. Supplementary movies are available at <https://doi.org/10.1017/jfm.2022.508>.

Funding. This material is based upon work supported by the National Science Foundation under grant no. 1936445. Research was sponsored in part by the University of Pittsburgh, Center for Research Computing, through the computing resources provided.

Declaration of interests. The authors report no conflict of interest.

Author ORCID*s*.

 Cheng-Nian Xiao <https://orcid.org/0000-0001-7788-8827>;

 Inanc Senocak <https://orcid.org/0000-0003-1967-7583>.

REFERENCES

- BILLANT, P. 2010 Zigzag instability of vortex pairs in stratified and rotating fluids. Part 1. General stability equations. *J. Fluid Mech.* **660**, 354.
- BILLANT, P. & CHOMAZ, J.-M. 2000 Experimental evidence for a new instability of a vertical columnar vortex pair in a strongly stratified fluid. *J. Fluid Mech.* **418**, 167–188.
- BROWAND, F.K. & WEIDMAN, P.D. 1976 Large scales in the developing mixing layer. *J. Fluid Mech.* **76** (1), 127–144.
- BUSSE, F.H. & CLEVER, R.M. 1979 Instabilities of convection rolls in a fluid of moderate Prandtl number. *J. Fluid Mech.* **91** (2), 319–335.
- CANTWELL, C.D., *et al.* 2015 Nektar++: an open-source spectral/hp element framework. *Comput. Phys. Commun.* **192**, 205–219.
- CLEVER, R.M. & BUSSE, F.H. 1974 Transition to time-dependent convection. *J. Fluid Mech.* **65** (4), 625–645.
- CLEVER, R.M. & BUSSE, F.H. 1977 Instabilities of longitudinal convection rolls in an inclined layer. *J. Fluid Mech.* **81** (1), 107–127.
- CORCOS, G.M. & SHERMAN, F.S. 1984 The mixing layer: deterministic models of a turbulent flow. Part 1. Introduction and the two-dimensional flow. *J. Fluid Mech.* **139**, 29–65.
- CRAIK, A.D.D. & LEIBOVICH, S. 1976 A rational model for Langmuir circulations. *J. Fluid Mech.* **73** (3), 401–426.
- CROW, S.C. 1970 Stability theory for a pair of trailing vortices. *AIAA J.* **8** (12), 2172–2179.
- DAUXOIS, T., FAUVE, S. & TUCKERMAN, L. 1996 Stability of periodic arrays of vortices. *Phys. Fluids* **8** (2), 487–495.

Speaker-wire vortices in stratified anabatic slope flows

- DELONCLE, A., BILLANT, P. & CHOMAZ, J.-M. 2011 Three-dimensional stability of vortex arrays in a stratified and rotating fluid. *J. Fluid Mech.* **678**, 482–510.
- FEDOROVICH, E. & SHAPIRO, A. 2009 Structure of numerically simulated katabatic and anabatic flows along steep slopes. *Acta Geophys.* **57** (4), 981–1010.
- GARCIA-VILLALBA, M. & DEL ALAMO, J.C. 2011 Turbulence modification by stable stratification in channel flow. *Phys. Fluids* **23** (4), 045104.
- HALL, P. & HORSEMAN, N.J. 1991 The linear inviscid secondary instability of longitudinal vortex structures in boundary layers. *J. Fluid Mech.* **232**, 357–375.
- HATTORI, Y., SUZUKI, S., HIROTA, M. & KHANDELWAL, M. 2021 Modal stability analysis of arrays of stably stratified vortices. *J. Fluid Mech.* **909**, A4.
- JULIEN, S., CHOMAZ, J.-M. & LASHERAS, J.-C. 2002 Three-dimensional stability of periodic arrays of counter-rotating vortices. *Phys. Fluids* **14** (2), 732–743.
- LE DIZÈS, S. & BILLANT, P. 2009 Radiative instability in stratified vortices. *Phys. Fluids* **21** (9), 096602.
- LI, F. & MALIK, M.R. 1995 Fundamental and subharmonic secondary instabilities of Görtler vortices. *J. Fluid Mech.* **297**, 77–100.
- MALLIER, R. & MASLOWE, S.A. 1993 A row of counter-rotating vortices. *Phys. Fluids A: Fluid Dyn.* **5** (4), 1074–1075.
- MIKSAD, R.W. 1972 Experiments on the nonlinear stages of free-shear-layer transition. *J. Fluid Mech.* **56** (4), 695–719.
- MIZAZAKI, T. & FUKUMOTO, Y. 1992 Three-dimensional instability of strained vortices in a stably stratified fluid. *Phys. Fluids A: Fluid Dyn.* **4** (11), 2515–2522.
- PIERREHUMBERT, R.T. 1986 Universal short-wave instability of two-dimensional eddies in an inviscid fluid. *Phys. Rev. Lett.* **57** (17), 2157.
- PIERREHUMBERT, R.T. & WIDNALL, S.E. 1982 The two- and three-dimensional instabilities of a spatially periodic shear layer. *J. Fluid Mech.* **114**, 59–82.
- PRANDTL, L. 1942 *Führer durch die Strömungslehre*. Vieweg und Sohn.
- PRANDTL, L. 1952 *Essentials of Fluid Dynamics: With Applications to Hydraulics, Aeronautics, Meteorology and other Subjects*. Blackie & Son.
- ROBINSON, A.C. & SAFFMAN, P.G. 1982 Three-dimensional stability of vortex arrays. *J. Fluid Mech.* **125**, 411–427.
- ROY, C., SCHAEFFER, N., LE DIZÈS, S. & THOMPSON, M. 2008 Stability of a pair of co-rotating vortices with axial flow. *Phys. Fluids* **20** (9), 094101.
- SCHMID, P.J. & HENNINGSON, D.S. 2001 *Stability and Transition in Shear Flows*. Springer.
- SHAPIRO, A. & FEDOROVICH, E. 2004 Unsteady convectively driven flow along a vertical plate immersed in a stably stratified fluid. *J. Fluid Mech.* **498**, 333–352.
- WINANT, C.D. & BROWAND, F.K. 1974 Vortex pairing: the mechanism of turbulent mixing-layer growth at moderate Reynolds number. *J. Fluid Mech.* **63** (2), 237–255.
- XIAO, C.-N. & SENOCAK, I. 2019 Stability of the Prandtl model for katabatic slope flows. *J. Fluid Mech.* **865**, R2.
- XIAO, C.-N. & SENOCAK, I. 2020a Linear stability of katabatic Prandtl slope flows with ambient wind forcing. *J. Fluid Mech.* **886**, R1.
- XIAO, C.-N. & SENOCAK, I. 2020b Stability of the anabatic Prandtl slope flow in a stably stratified medium. *J. Fluid Mech.* **885**, A13.
- XIAO, C.N. & SENOCAK, I. 2022 Impact of stratification mechanisms on turbulent characteristics of stable open-channel flows. *J. Atmos. Sci.* **79** (1), 205–225.